Mesoporous Zr-G-C3N4 Sorbent as an Exceptional Cu (II) Ion Adsorbent in Aquatic Solution: Equilibrium, Kinetics, and Mechanisms Study

Lotfi Khezami, Abueliz Modwi, Kamal K. Taha, Mohamed Bououdina, Naoufel Ben Hamadi, Aymen Amine Assadi

Lotfi Khezami, Abueliz Modwi, Kamal K. Taha, Mohamed Bououdina, Naoufel Ben Hamadi, et al.. Mesoporous Zr-G-C3N4 Sorbent as an Exceptional Cu (II) Ion Adsorbent in Aquatic Solution: Equilibrium, Kinetics, and Mechanisms Study. Water, 2023, 15 (6), pp.1202. 10.3390/w15061202 . hal-04087553 water

MDPI

Article

Mesoporous Zr-G-C_3N_4 Sorbent as an Exceptional Cu (II) Ion Adsorbent in Aquatic Solution: Equilibrium, Kinetics, and Mechanisms Study

Lotfi Khezami [1,*], Abueliz Modwi [2], Kamal K. Taha [3], Mohamed Bououdina [4], Naoufel Ben Hamadi [1] and Aymen Amine Assadi [5,*]

[1] Chemistry Department, College of Science, Imam Mohammad Ibn Saud Islamic University (IMSIU), P.O. Box 5701, Riyadh 11432, Saudi Arabia
[2] Department of Chemistry, College of Science and Arts at Al-Rass, Qassim University, Buraydah 52571, Saudi Arabia
[3] Chemistry & Industrial Chemistry Department, College of Applied & Industrial Sciences, Bahri University, Khartoum 11111, Sudan
[4] Department of Mathematics and Sciences, College of Humanities and Sciences, Prince Sultan University, Riyadh 11586, Saudi Arabia
[5] École Nationale Supérieure de Chimie de Rennes (ENSCR), Université de Rennes, UMR CNRS 6226, 11 Allée de Beaulieu, 35700 Rennes, France
* Correspondence: lhmkhezami@imamu.edu.sa (L.K.); aymen.assadi@ensc-rennes.fr (A.A.A.)

Abstract: A mesoporous Zr-G-C_3N_4 nanomaterial was synthesized by a succinct-step ultrasonication technique and used for Cu^{2+} ion uptake in the aqueous phase. The adsorption of Cu^{2+} was examined by varying the operating parameters, including the initial metal concentration, contact time, and pH value. Zr-G-C_3N_4 nanosorbent displays graphitic carbon nitride (g-C_3N_4) and ZrO_2 peaks with a crystalline size of ~14 nm, as determined by XRD analysis. The Zr-G-C_3N_4 sorbent demonstrated a BET-specific surface area of 95.685 m^2/g and a pore volume of 2.16×10^{-7} $m^3 \cdot g^{-1}$. Batch mode tests revealed that removing Cu (II) ions by the mesoporous Zr-G-C_3N_4 was pH-dependent, with maximal removal achieved at pH = 5. The adsorptive Cu^{2+} ion process by the mesoporous nanomaterial surface is well described by the Langmuir isotherm and pseudo-second-order kinetics model. The maximum adsorption capacity of the nanocomposite was determined to be 2.262 $mol \cdot kg^{-1}$ for a contact time of 48 min. The results confirmed that the fabricated mesoporous Zr-G-C_3N_4 nanomaterial is effective and regenerable for removing Cu^{2+} and could be a potent adsorbent of heavy metals from aqueous systems.

Keywords: Zr-doped G-C_3N_4; wastewater treatment; mineral pollutant; catalysts regeneration

check for updates

Citation: Khezami, L.; Modwi, A.; Taha, K.K.; Bououdina, M.; Ben Hamadi, N.; Assadi, A.A. Mesoporous Zr-G-C_3N_4 Sorbent as an Exceptional Cu (II) Ion Adsorbent in Aquatic Solution: Equilibrium, Kinetics, and Mechanisms Study. *Water* **2023**, *15*, 1202. https://doi.org/10.3390/w15061202

Academic Editor: Hai Nguyen Tran

Received: 6 February 2023
Revised: 16 March 2023
Accepted: 16 March 2023
Published: 20 March 2023

1. Introduction

Numerous harmful heavy metals are released to the environment due to industrial wastewater discharges. Even at low concentrations, they contribute significantly to pollution and endanger human health. Simultaneously, some of them, such as silver and copper, are valuable and may be recycled and used in various applications [1,2]. Toxic heavy metals found in liquid effluents, such as copper (II), are persistent, nonbiodegradable, and bioaccumulated, hence posing a severe threat to natural human health and the environment [3–5]. Many adsorbents were modified or functionalized to adsorb copper ions, for instance, 48.6, 25, 105.3, 86.95, and 31 mg/g were eliminated using polyethylenimine modified wheat straw [6], chitosan/poly (vinyl alcohol) beads functionalized with poly (ethylene glycol) [7], hematite (α-Fe_2O_3) iron oxide-coated sand [8], chitosan–montmorillonite composite [9] and chitosan@TiO_2 composites [10], respectively.

Mining and electroplating industries, for example, discharge aqueous effluents containing high amounts of heavy metals such as uranium, mercury, cadmium, lead, and copper into the environment [11,12]. Cu (II) concentrations in wastewater produced by industrial activities are frequently high [13]. The heavy metal Cu (II) can settle down in the human body and cause significant health problems in the skin, liver, heart, and brain. Cu (II) was found to be carcinogenic [13,14], especially when its concentration exceeded the (∼20 μM) limit set by the U.S. Environment Protection Agency (EPA) for potable water [15]. As a result, extensive efforts have been devoted to removing Cu (II) from the aquatic environment.

Recently researchers are showing great fascination with graphitic carbon nitride (g-C_3N_4) due to its simple synthesis from the most earth-abundant elements (carbon and nitrogen) to make strong covalent bonds in its conjugated layer structure [16]. It is appealing, by virtue of the high chemical and thermal stability narrow-bandgap energy 2.7 eV (460) nm and efficient visible-light absorption. Additionally, the exceptional delocalized conjugated system of the stacked graphitic C_3N_4 layers, which are interconnected with nitrogen-containing functional groups, are capable of bonding to pollutants during the adsorption of photocatalysis [17]. Nevertheless, C_3N_4 suffers some drawbacks, including high electron–hole recombination, a low absorption coefficient, and a low specific surface area, which are mainly overcome by doping with metal and metal oxides [18].

Chemical precipitation, ion exchange, reverse osmosis, nanofiltration, and adsorption are some of the heavy metal removal processes that are commonly used [19]. Most of these approaches are not suited for small-scale companies due to their large capital expenditures. The adsorption process is the most effective method of eliminating ecologically harmful and hazardous organic–inorganic compounds from the environment [20–22]. Further, the development of cost-effective adsorbents for heavy metal removal from wastewater relies on the fabrication of nanostructured materials with enhanced properties—primarily high surface area—that play an essential role in the adsorption process. Numerous studies have focused particularly on metal oxides and composites based on metal oxides to remove heavy metals from aqueous solutions [23–26].

Interestingly, both precursors used for the Zr-G-C_3N_4 fabrication are biocompatible where ZrO_2 finds medical application in dentistry and biomedical implants without adverse reactions [27,28], while G-C_3N_4 is employed as an anode in microbial fuel cells [29] and human-safe antimicrobial agents [30]. Therefore, this paper aims to prepare a harmless Zr-G-C_3N_4 nanosorbent to treat wastewater contaminated with copper ions, one of the most prevalent hazardous heavy metals. Using thermal pyrolysis, Zr-G-C_3N_4 sorbent was fabricated. XRD, SEM/EDX, and FTIR analyses were carried out to examine nanomaterials' structure, morphology and chemical composition, specific surface and pore size, and functional groups. The effect of operational parameters such as contact time and pH on the adsorption capacity of Cu ions was investigated. Moreover, kinetic and isothermal adsorption tests were conducted. A plausible mechanism of Cu^{2+} ion adsorption onto Zr-G-C_3N_4 sorbent was discussed and proposed.

2. Experimental

2.1. Nanomaterial Fabrication, Morphological, and Structural Characterization

Mesoporous Zr-G-C_3N_4 sorbent was already synthesized [18] using a straightforward one-step ultrasonication technique.

Using a Bruker D8 Advance X-ray diffractometer (Bruker AXS, Karlsruhe, Germany) with Cu-Ka1 radiation and k = 1.5406 at a scan speed of 0.002/per second, the structural characteristics of the Zr-G-C_3N_4 sorbent were investigated. The surface texture of the manufactured sorbent was estimated via N2 adsorption at 77 K using ASAP 2020 HD 88 equipment. Prior to each investigation, the ZnO sample was outgassed at 250 °C for 6 h by a constant helium current flow. On a scale of 400–4000 cm^{-1}, the FT-IR spectra of the ZOCN mesosorbent before and after MG dye elimination were monitored with a Nicolet 5700 FT-IR spectrophotometer. The Cu^{2+} ion content was measured on a Shimadzu 680 A or a Perkin-Elmer 603 atomic absorption spectrometer with a hallow cathode lamp and a deuterium background corrector, at respective resonance line using an air–acetylene flame.

On the other hand, a Hitachi S4700 Scanning electron microscopy (SEM) (Anhui, China) operating at a 25 kV and a Tecnai G20 TEM (Houston, TX, USA) operating at a 200 kV were used for morphological observations and elemental chemical composition.

2.2. Cu^{2+} Ion Removal Experiments

The efficiency of the produced nanomaterial for removing Cu metal ions was realized in a batch mode reactor at room temperature. A total of 10 mg of Zr-G-C_3N_4 sorbent was added to a series of Erlenmeyer flasks containing 25 mL synthetic solutions with different starting concentrations, C_0 (5 to 200 ppm), 27 °C, and a pH ranging from 1 to 8. The flasks were firmly sealed to prevent evaporation, and the suspension was constantly agitated at 420 rpm for 24 hrs. The supernatant solution of Cu ions and Zr-G-C_3N_4 sorbent was separated by 10 min centrifugation at 2500 rpm. In the meantime, the remaining Cu^{2+} ion concentrations, C_e, were analyzed by atomic absorption spectroscopy (AAS). The ultimate adsorptive capacity (qe) relative to the starting and equilibrium concentrations was calculated using the following equation:

$$q_e = \frac{V}{m}(C_0 - C_e) \tag{1}$$

where m (in g) is the Zr-G-C_3N_4 adsorbent mass, V (in L) is the solution volume.

To specify the period of time needed to achieve sorption equivalency for Cu^{2+} metal ions onto Zr-G-C_3N_4 sorbent, the removal process was examined at various predetermined contact times from 5 to 1440 min. At room temperature, the Cu^{2+} metal ion kinetics rate was provided at a constant Zr-G-C_3N_4 sorbent mass of 60 mg and 150 mL initial copper metal solution concentration of about 60 ppm. The remaining Cu ion concentration (C_t) was measured using AAS, and the adsorption kinetic models are mentioned in the Results section.

The Cu^{2+} ion concentration was determined and utilized to specify the adsorption capacity at time t (q_t) and the percentage removal (%R), which were estimated using the following expressions:

$$q_t = \frac{V}{m}(C_0 - C_t) \tag{2}$$

$$\%R = (C_0 - C_t)\frac{100\%}{C_0} \tag{3}$$

At pH > 6, the filtrate was acidified with dilute HNO_3 prior to Cu^{2+} ion concentration by AAS.

3. Results and Discussion

3.1. Composition Phase and Surface Characteristics of Mesoporous Zr-G-C_3N_4 Sorbent

The recorded XRD pattern of the Zr-G-C_3N_4 sorbent is shown in Figure 1a. The peaks at 24.00° (110), 28.22° (−111), 31.35° (111), 34.07° (200), 35.27° (002), 40.64° (120), 44.80° (211), 49.24° (220), and 50.09° (022) are indexed within a monoclinic crystal structure of the ZrO_2 phase (JCPDS card No. 00-37-1484) [31,32]. The remaining peaks located at 13.0° (100) and 27.58° (002) correspond to the layered two-dimensional structure of the G-C_3N_4 phase (JCPDS card No 87-1526 [33]. No additional peaks are detected, except ZrO_2 and g-C_3N_4, indicating the formation of a pure biphasic composite composed of the ZrO_2 phase with a monoclinic crystal structure and the g-C_3N_4 phase with a layered two-dimensional structure. The crystallite sizes determined by the Scherrer formula [34] using the most intense reflection (002) for G-C_3N_4 and (−111) for ZrO_2 are found to be 7.94 and 13.95 nm, respectively. Figure 1b illustrates the N_2 sorption–desorption isotherm of the Zr-G-C_3N_4 sorbent. The nanostructure's isotherm is of type IV, suggesting the existence of mesopores throughout the material resulting from the narrow hysteresis loop generation [35,36]. The Zr-G-C_3N_4 sorbent exhibits a specific surface area of 95.7 $m^2 \cdot g^{-1}$ and a pore volume of

$0.000000216\ m^3 \cdot g^{-1}$. The relatively high surface area is expected to improve the sorption capability of the as-fabricated mesoporous Zr-G-C_3N_4 nanocomposite [18].

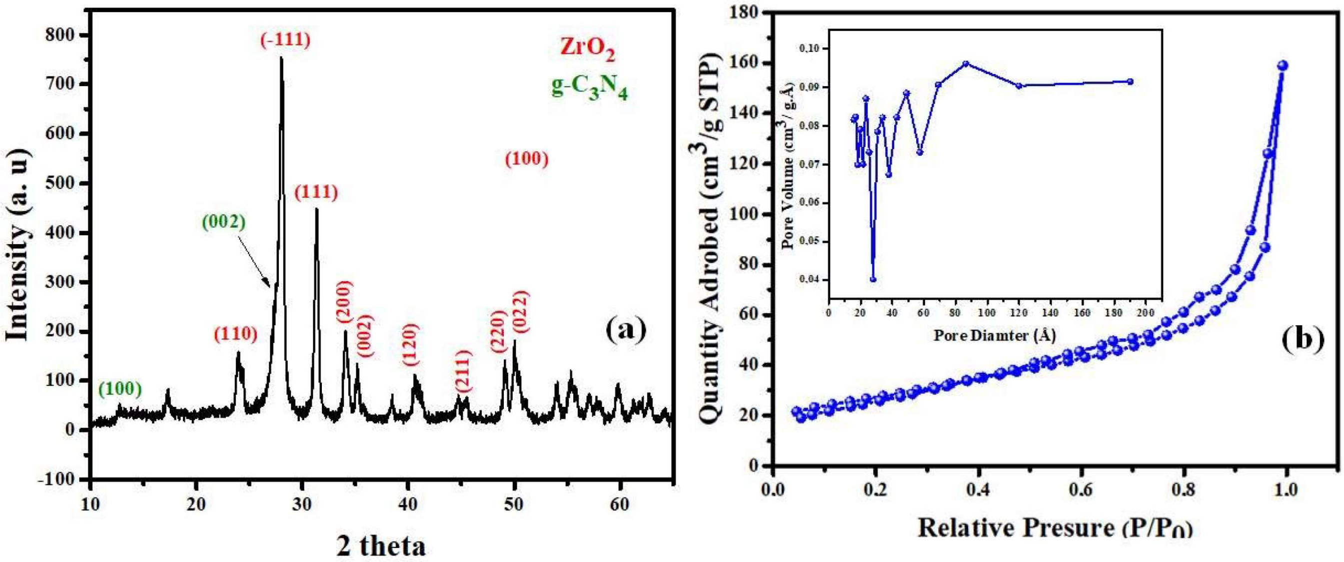

Figure 1. (**a**) XRD pattern; (**b**) N_2 sorption–desorption isotherm of Zr-G-C_3N_4 sorbent. The inset in (**b**) presents the pore size distribution.

Figure 2 illustrated SEM morphological observations with EDX chemical analysis and elemental mapping of the nanocomposite before the adsorption process.

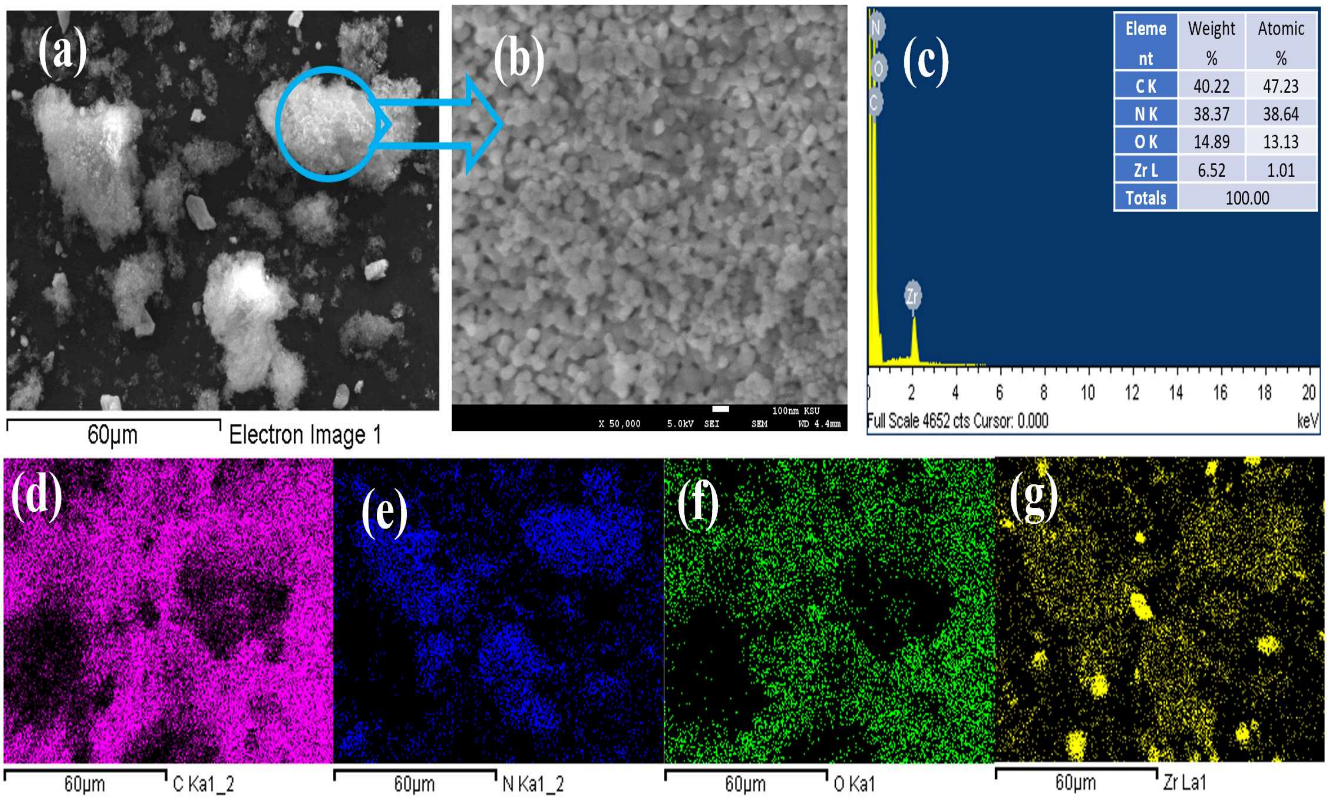

Element	Weight %	Atomic %
C K	40.22	47.23
N K	38.37	38.64
O K	14.89	13.13
Zr L	6.52	1.01
Totals	100.00	

Figure 2. (**a**) SEM image and (**c**) EDX spectrum for element composition; (**b**,**d**–**g**) elemental mapping of C, N, O, and Zr, respectively, in Zr-G-C_3N_4 nanocomposite.

Figure 2a reveals smaller elongated particles with smooth surfaces alongside larger aggregates formed by spherical-shaped particles in the nanoscale with homogenous size distribution (Figure 2b). The nanoparticles are interconnected, forming a mesoporous network nanostructure all over the material, generated from the thin hysteresis loop spawning, which is convenient with the BET analysis manifesting a type II isotherm [18].

The EDS spectrum of Zr-G-C_3N_4 (Figure 2c) contains the peaks related to C, N, O, and Zr, confirming once again that the purity of the as-fabricated nanocomposite material made of graphitic carbon nitride and zirconium oxide corroborates the literature [18,19], and EDS elemental mapping indicates homogenous distribution Figure 2d–g.

3.2. Adsorption Measurements of Zr-G-C_3N_4 sorbent

3.2.1. Impact of Adsorption Time

Figure 3a depicts the effect of contact time on the % removal of Cu^{2+} ions at room temperature. The adsorption of copper ions onto the Zr-G-C_3N_4 sorbent has been examined during agitating durations varying from 5 to 1440 min for an initial concentration of 0.708 mmol/L and 27 °C. The half-amount of metal ions eliminated was attained in 22 min, and 97% of the adsorbate was completely removed in the process. Owing to the multiple active sites on the Zr-G-C_3N_4 nanomaterial surface, the initial adsorption rate is significantly high, reaching a value of h_0 = 4.45 mg/(g.min).

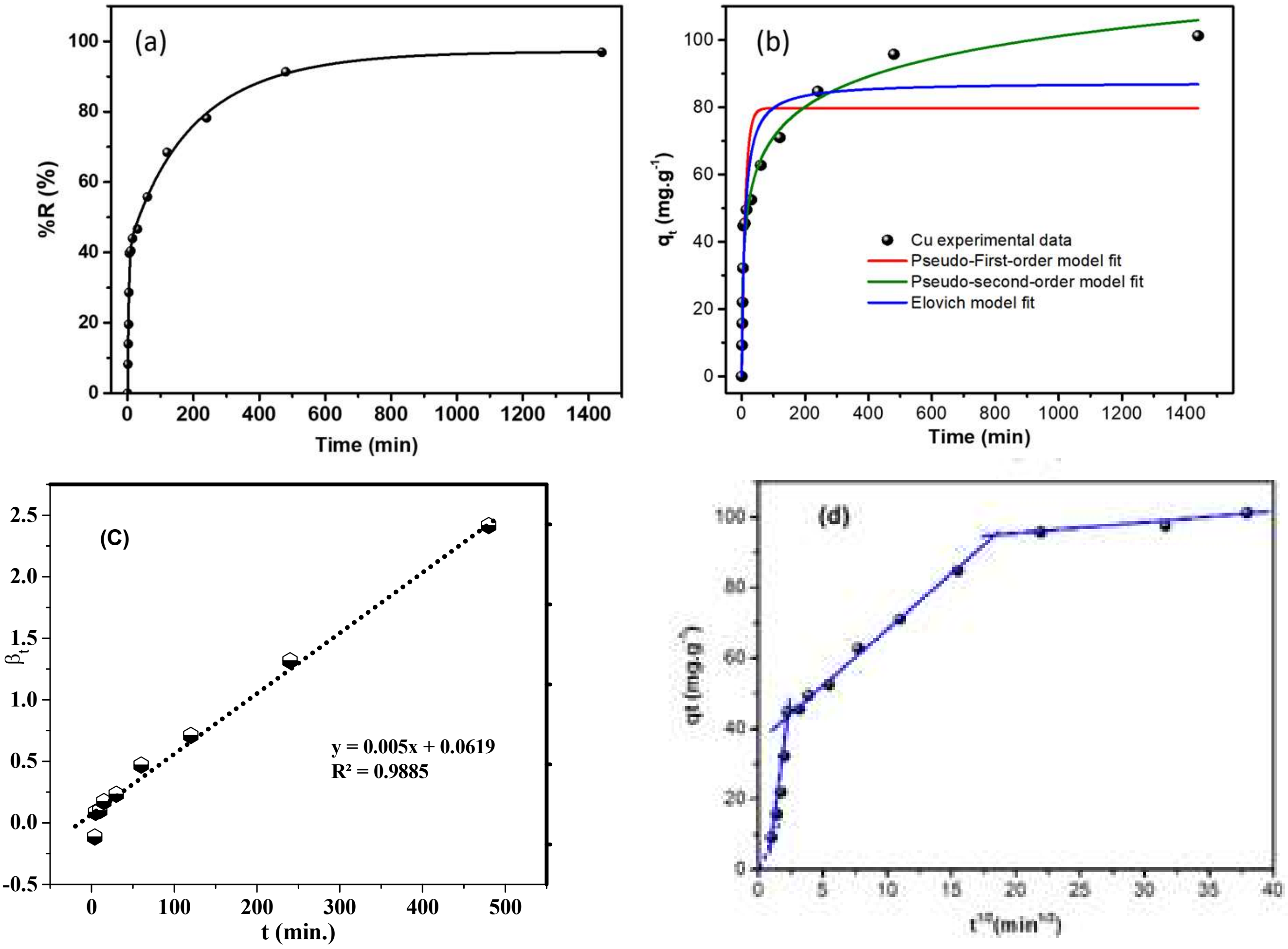

Figure 3. (**a**) Impact of adsorption time and (**b**) fitting experimental data with different nonlinear kinetics models; (**c**) Boyd model and (**d**) IPDT model for Cu^{2+} metal ion uptake onto the sorbent Zr-G-C_3N_4, using a nonlinear trend.

3.2.2. Kinetic Study

In order to obtain an insight into the process that governs the adsorption of Cu ions, the kinetic measurement is often conducted using various kinetic models (Table 1). The obtained experimental data may be well fitted by the pseudo-first-order (PFO), (the pseudo-second-order (PSO), the Elovich, and the intraparticle diffusion (IPD) models as depicted by the nonlinear model fittings in Table 1 and Figure 4.

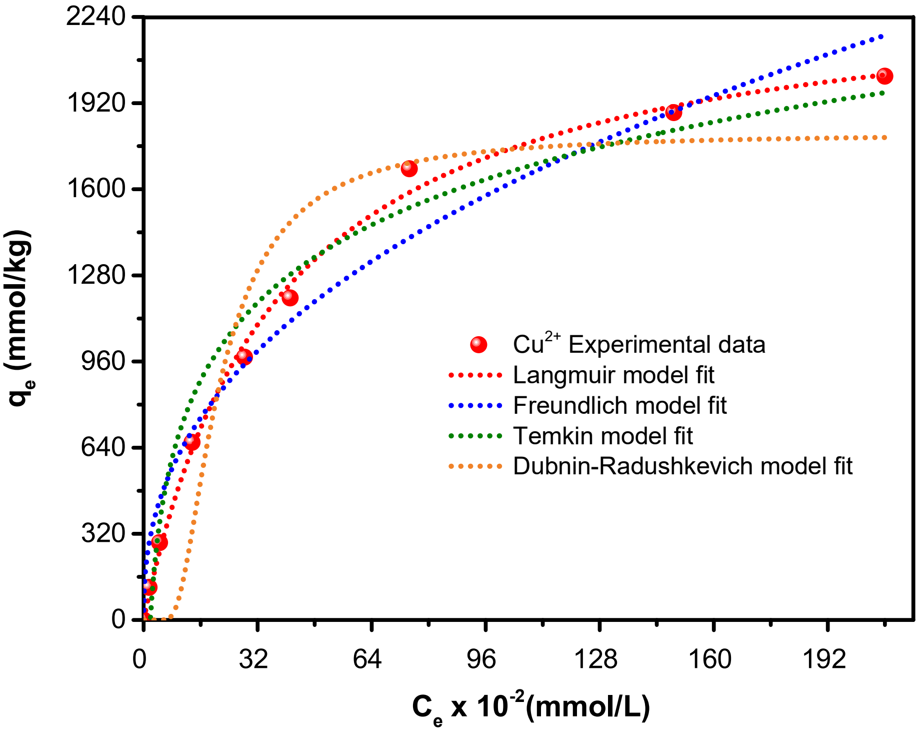

Figure 4. The nonlinear illustration of the equilibrium experimental data.

The PFO kinetic model (Equation (4)) demonstrates the presence of proportionality between the binding capability and the number of available active sites [20]. From the PFO graph (Figure 3), the rate constant k_1 and the adsorbed amount during the contact time were 1.4×10^{-3}·min^{-1} and 51.5 mg·g^{-1} in turn. The difference in the adsorbed amount compared to the experimental data and the lesser correlation coefficient value (Table 1) indicates that the PFO kinetic model is inappropriate to describe this process. The PSO kinetics model (Figure 3 and Equation (5)) assumes the chemisorption process as the rate-limiting phase accompanying the valence electrons' involvement between the nanomaterial and the pollutant [21].

The PSO model rate constant (k_2) and ultimate adsorbed amount of Cu^{2+} ions were 5.6×10^{-3} g·mg^{-1}·min^{-1} and 90 g·mg^{-1}, respectively. The almost-equal values of the calculated (90 g·mg^{-1}) and experimentally (87 g·mg^{-1}) adsorbed amount and the large rate constant (k_2), as well as the strong correlation coefficient close to the unit (i.e., 0.9984), demonstrate that adsorption follows the PSO kinetic model (e.g., Table 1 and Figure 3) [20].

Table 1. Kinetics models' parameters for the removal of Cu (II) by Zr-G-C_3N_4.

Kinetics Model	Linear and Nonlinear Kinetic Equations	Equation No.	Refs.	Parameters	Values
Pseudo-first-order	$q_t = q_e\,(1 - e^{-k_1 t})$	(4)	[37,38]	q_m (mg·g^{-1})	51.5
				k_1 (min^{-1})	1.4×10^{-3}
				R^2	0.8207
Pseudo-second-order	$q_t = \frac{k_2 q_e^2 t}{1+k_2 q_e t}$	(5)	[37]	$q_{m\ (exp.)}$ (mg·g^{-1})	87
				$q_{m\ (cal.)}$ (mg·g^{-1})	90
				k_2 (g·mg^{-1}·min^{-1})	5.6×10^{-3}
				h_0 (mg·(g^{-1}·min^{-1}))	4.65
				$t_{1/2}$ (min^{-1})	21.95
				R^2	0.9984
Elovich	$q_t = \frac{1}{\beta}\ln(1 + \alpha\beta t)$	(6)	[39]	β (g·mg^{-1})	0.0863
				α (mg·g^{-1}·min^{-1})	57.37
				R^2	0.9687
Intraparticle diffusion	$q_t = k_{dif} t^{1/2} + C$	(7)	[39]	k_{dif1} (mg·g^{-1}·min$^{1/2}$)	70.89
				C_1 (mg·g^{-1})	41.76
				R^2	0.9737
				k_{dif2} (mg·(g^{-1}·min$^{-1/2}$))	1.14
				C_2 (mg·g^{-1})	81.88
				R^2	0.9527
				k_{dif3} (mg·(g^{-1}·min$^{-1/2}$))	0.046
				C_3 (mg·g^{-1})	115.32
				R^2	0.9612
Film diffusion	$-0.4977 - \ln(1 - F)$ $F = \frac{q_t}{q_e}$	(8)	[40]	k (min^{-1})	5.00×10^{-3}
				D_i (cm^{-2}·g^{-1}·min^{-1})	9.166×10^{-9}
				R^2	0.9885

Notes: q_t: adsorption capacity at time (t). q_e: adsorption capacity at equilibrium. C_0: initial concentration. C_e: equilibrium concentration. k_1: PFO rate constant. k_2: PSO rate constant. β: activity coefficient. ε: the Polanyi potential. *kid*: IPDT diffusion rate constant. *C*: diffusion layer thickness. *Di*: diffusion coefficient.

This finding is in accordance with Cu^{2+} ion uptake on modified nanocomposites [22]. The PSO kinetic model was used to derive the initial rate of sorption $h_0 = k_2 \cdot q_e{}^2$ and the half-sorption time $t_{1/2} = 1/(k_2 \cdot q_e)$ as the time needed for eliminating the half amount of the equilibrium value. Time is usually used as an indicator of the sorption rate. The high initial rate of adsorption h_0 (4.65 mg/(g·min)) and the briefer half-duration of adsorption (21.95 min) indicate that Cu^{2+} ions are adsorbed at a high rate [23]. In addition, the experimental data were modeled by the Elovich equation (Equation (6)) (Figure 3b), and the initial rate a and β values were 0.0863 and 57.37, respectively. Moreover, the correlation between the observed data and the Elovich equation is also confirmed by the R^2 value (i.e., 0.9687) [24]. The good agreement with the Elovich model supports that the adsorption mechanism is governed by chemisorption, supporting the PSO kinetic model [24,25]. Danesh et al. studied the elimination of Cu^{2+} ions by modified nanocomposites (GFLE) and proved that experimental data are well described by the second-order-kinetics model.

3.2.3. Intraparticle Diffusion/Transport Model (IPDT)

The IPDT (Equation (8)) may move the adsorbed Cu^{2+} metal ions from the preponderance of the solution to nanoparticles' interface. This process presents a step in the adsorption mechanism that acts as a restraint. Weber and Morris' diffusion model verifies the potential of intraparticle dissemination (Table 1) [24,25]. The C and k_{dif} model constants' values can be derived from the intercept and slope of q_t vs. $(t)^{1/2}$ linear plot, respectively (Figure 3d). Since q_t changes linearly with $t^{1/2}$, the uptake of Cu^{2+} metal ions at the Zr-G-C_3N_4 nanomaterial surface verifies the plausibility of the IPDT kinetic model. In addition, the regression coefficient (R^2) close to the unit) identifies the IPDT mode of diffusion. Moreover, C is a parameter measuring the thickness of the border layer. The substantial effect of the solution border layer on the uptake process is validated by the higher constant values given in Table 1 [23–25].

Moreover, the primary adsorption step has a greater rate than the final step, as affirmed by the values of k_{dif} shown in Table 1. The rapid rate of the primary step may be attributed to the transfer of Cu^{2+} metal ions through the solution up to the nanomaterials' external surface via the border layer. Simultaneously, the subsequent stage manifests the final equilibrium step as the IPDT drops due to the less solute concentration gradient resulting from the dwindling number of mesopores available for diffusion. In addition, the increased value of the C parameter in the final step suggests the existence of a border coating impact [23], confirming the role of intraparticle diffusion in the removal of Cu^{2+} metal ions by Zr-G-C_3N_4 [40].

The Boyd model is assessed for chemisorption kinetics to confirm the film diffusion influence. It is expressed by the formula given in Equation (8) [41]. The term F represents the ratio of metal ions adsorbed at any time t (min), and Bt is a mathematical function of F. In case the plot of Bt versus t is linear and passes through the origin, the rate of mass transfer is controlled by pore diffusion. Else a nonlinear plot—or linear without passing through the origin—the film diffusion or chemical reaction controls the adsorption rate [42]. In accordance, Bt vs. t graph that does not pass through the origin (Figure 3c) denotes a film diffusion or chemical reaction control on the adsorption rate [43].

The diffusion coefficient D_i can be calculated by the following formula [44]:

$$D_i = \frac{B}{\pi A}$$

where B is the slope of Bt vs. t in min^{-1}, and A is the adsorbent's surface area in $cm^2 \cdot g^{-1}$. The calculated D_i value is 9.166×10^{-9} $cm^{-2} \cdot g^{-1} \cdot min^{-1}$ which is outside the 10 to 11×10^{-11} $cm^{-2} \cdot g^{-1} \cdot min^{-1}$ range quantified for the intraparticle phenomenon. This corroborates the film diffusion involvement in the adsorption process [44] and that intraparticle diffusion is not the sole rate-controlling step of the process [45].

3.2.4. Uptake Isotherms of Copper Ions

The uptake isotherms reveal the affinity of the nanomaterial and its surface characteristics. Consequently, they are commonly employed to compare the ultimate adsorbed amount (q_m) of the adsorbent to the pollutants in wastewater. Various empirical and semiempirical equations are used to describe the behavior of the adsorption process until equilibrium is reached. Among these equations, the Langmuir model (Equation (9)) presumes that all active sites of the homogeneous surfaces possess equivalent adsorption energies, where the interaction between the sorbed species is insignificant. Table 2 presents the nonlinear form of this isotherm, where q_e represents the number of Cu^{2+} metal ions adsorbed and q_m and b characterize the complete monolayer packing and the Langmuir constant, respectively [46].

Furthermore, Freundlich's model (Equation (10)) is a semiempirical equation applicable to multilayer filling on heterogeneous surfaces characterizing a nonideal uptake [11].

These equations [14] rely upon the amount of adsorbate per gram of adsorbent (q_e) to the solute equilibrium concentration (C_e) [30]. The n and k_f Freundlich model's constants describe the adsorption intensity and relative uptake capability. Moreover, they establish the capacity of adsorption and the nonlinear behavior representing the concentration change and solution. The adsorption intensity depends on the values of n; i.e., $n < 1$ for low; $1 < n < 2$ for moderate, and $2 < n < 10$ for high adsorption capacities, respectively [47].

Table 2. Different equilibrium isotherms' constants for Cu^{2+} ion adsorption by Zr-G-C_3N_4 nanomaterial.

Equilibrium Model	Linear and Nonlinear Equilibrium Equations	Equation No.	Refs.	Parameters	Cu^{2+}
Langmuir	$qe = \frac{qmbC_e}{1+bC_e}, R_L = \frac{1}{1+a_L C_0}$	(9)	[26]	q_m (mol·kg^{-1})	2.262
				b (L·mol^{-1})	5.5×10^{-6}
				R_L	0.9514
				R^2	0.9907
Freundlich	$q_e = K_F(C_e)^{1/n}$	(10)	[48]	n	1.73
				k_F mmol·g^{-1}$\left(\text{mmol·L}^{-1}\right)^{-0.578}$	9.87
				R^2	0.9634
Temkin	$q_e = \frac{RT}{\beta_T} Ln(K_T C_e)$	(11)	[49]	β_T (J·mol^{-1})	563.2
				k_T (L·mmol^{-1})	5.85
				R^2	0.9612
Dubinin–Radushkevich	$q_e = q_m \exp(-\beta\varepsilon^2)$, $\varepsilon = (RTln(1 + \frac{1}{C_e}))^2$ $E = \frac{1}{\sqrt{2\beta}}$	(12)	[50]	β (mol^2·J^{-2})	1.95×10^{-8}
				q (mol·kg^{-1})	18.6
				E (J·mol^{-1})	5064
				R^2	0.9864

The Temkin isotherm (Equation (11)) compensates for solute–solute indirect interaction in the adsorption process, where the molecules' adsorption heat linearly decreases inversely proportional to the layers' coverage [31]. Table 2 provides the linear and nonlinear equations for the Temkin model. The coefficients β_T and K_T are, sequentially, the Temkin isotherm energy and constant.

The same table illustrates the Dubinin–Radushkevich model (D-R)'s linear and nonlinear expressions (Equation (12)) [51] as a final stage, where $\boldsymbol{\beta}$ is related to the adsorption energy in mol^2/kJ^2, and ε (*RTln(1 + 1/Ce)*) is the Polanyi potential in kJ/mol. The coefficient $\boldsymbol{\beta}$ value allows for the determination of the mean value of adsorption activation energy, $\boldsymbol{E} = \frac{\mathbf{1}}{\sqrt{\mathbf{2}\boldsymbol{\beta}}}$, and pinpoints whether adsorption nature is a physical or chemical process [32]. The nonlinear uptake isotherms of Cu^{2+} metal ions on the Zr-G-C_3N_4 nonmaterial surface are displayed in Figure 4, respectively.

The best-described isotherm model for Cu^{2+} metal ions' equilibrium data is mainly evaluated based on the value of R^2 shown in Table 2. This table shows that the Langmuir isotherm has the highest regression factor value (0.9907) and the maximum q_m, indicating the compliance of the adsorption mechanism. The Langmuir model's key characteristics are evaluated through the separation coefficient, R_L, to examine the isotherm's applicability, as expressed in Table 2.

The R_L values prescribe the adsorption isotherm behavior as linear, favorable, unfavorable or irreversible if ($R_L = 1$), ($0 < R_L < 1$), ($R_L > 1$), or ($R_L = 0$) respectively [17,29,32]. The results given in Table 2 reveal a favorable isotherm (i.e., $R_L = 0.9514$), manifesting that the Cu ions' adsorption follows the Langmuir model. The obtained values demonstrate that the D-R model concurs with the elimination procedure, as confirmed by the higher value of r^2 (0.9864) and the significant adsorption capacity of Cu^{2+} metal ions (118.3 mg/g), and the energy amplitude is about 5.063 kJ·mol^{-1} [22,32–34]. Similarly, the coefficient (R^2) corresponds to the Freundlich equilibrium model, which is more significant than 0.96, agreeing well with the obtained experimental results. This finding can be sustained by the n-value amplitude (i.e., 1.73), which suggests a moderately good adsorption capacity. Moreover, the negative free energy value suggests a spontaneous physisorption uptake process (Table 2).

In this study, the Elovich model advocated that the adsorption of copper ions on the surface of the nanomaterial accrues under the chemisorption process. This result, together with the experimental data fitting to the Langmuir isotherm and the PSO kinetics model, indicates that the adsorption process of Cu^{2+} ions onto Zr-G-C_3N_4 nanomaterial involves a chemisorption mechanism. This is in agreement with the chemisorption of Cu(II) ions on modified chitosan [52], magnetite (Fe_3O_4) [53], activated carbon [54], and fly ash-derived zeolites [55] as examples.

3.2.5. The Impact of pH on Cu^{2+} (II) Ion Uptake

The impact of pH on Cu^{2+} metal ion removal efficiency is a critical aspect of the uptake process. It modifies the active sites on the Zr-G-C_3N_4 sorbent surface, which is competent for Cu coordination and the solubility of Cu ions in the aqueous solution. Depending on the solution's pH, the species of copper present include: Cu^{2+}, $Cu(OH)^+$, $Cu(OH)^0{}_2$, $Cu(OH)_3{}^-$, and $Cu(OH)_4{}^{2-}$ [56]. To determine the optimal pH for eliminating Cu^{2+} metal ions, the pH value varies from 1 to 8. Figure 5 illustrates the effect of initial pH on the uptake of the tested metal ions, and the results indicate that the best uptake capability is attained at pH 5 (43.37 mg g^{-1}). The amount of Cu^{2+} ions removed increases significantly at pH = 5. This is due to the copper ions precipitation as $Cu(OH)_2(s)$ at pH > 5 their existence in the hydrolyzed forms $Cu(OH)^0{}_2$, $Cu(OH)_3{}^-$, and $Cu(OH)_4{}^{2-}$ at higher pH values.

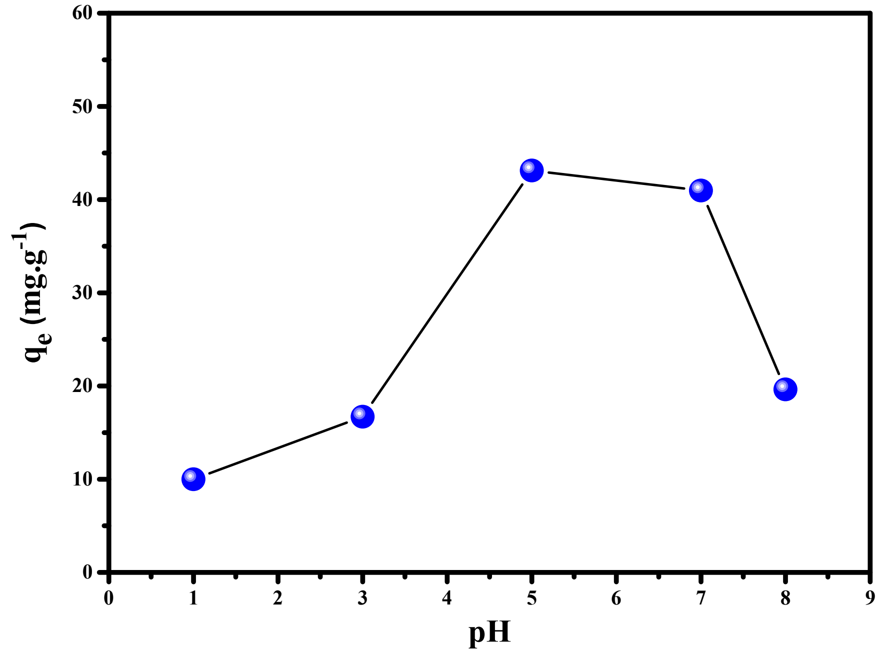

Figure 5. The pH impact on the uptake rate of Cu^{2+} metal ions by Zr-G-C_3N_4 nanomaterial.

At lower pH values, more hydrogen protons subsist to protonate active species on Zr-G-C_3N_4 nanomaterial surfaces and compete with Cu^{2+} ions in the suspension, which corroborates previous studies in the literature [57–60]. In addition, according to earlier studies, Cu^{2+} ions are only accessible in the divalent state at pH values below 5.0. Furthermore, it is important to highlight that there are numerous neutral hydrolysis species at pH 7.0 and above.

3.2.6. Uptake Mechanism of Copper Ions

To suggest a plausible uptake mechanism of Cu^{2+} ions on Zr-G-C_3N_4, Fourier transmission infrared spectra and EDS elemental mapping were recorded before and after the adsorption process. The FTIR spectrum of Zr-G-C_3N_4 before adsorption (Figure 6) reveals a broad band around 3266 cm^{-1}, which was ascribed to the stretching vibration of –OH groups of physically sorbed H_2O and the terminal amino groups on the Zr-G-C_3N_4 nanomaterial surface [40]. The band located at 887 cm^{-1} is assigned to the triazine ring mode. Further, the bands located at 1256, 1329, and 1429 cm^{-1} correspond to the bridged aromatic C–N stretching modes [41]. After Cu ion uptake, important modifications were noticed in the FTIR spectrum, as displayed in Figure 7. The band centered around 3266 cm^{-1} was less broadened, while the triazine ring mode band at 887 cm^{-1} shifted slightly to 881 cm^{-1}.

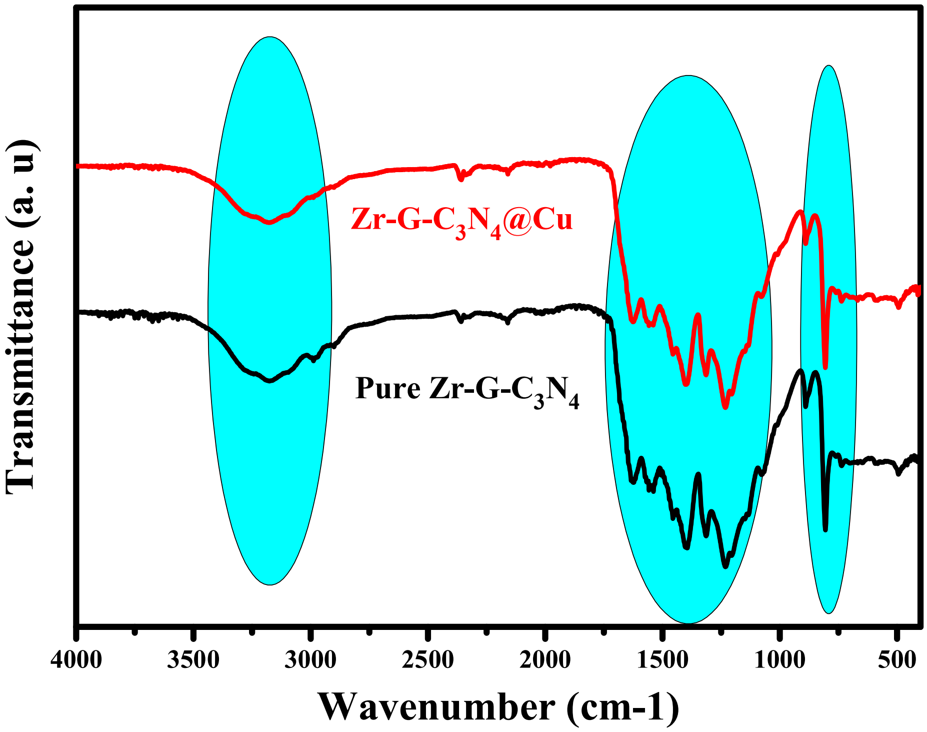

Figure 6. FTIR spectra before and after Cu^{2+} adsorption onto the surface of Zr-G-C_3N_4 nanomaterial.

Figure 7 illustrates SEM morphological observations with EDX chemical analysis and elemental mapping of the nanocomposite after the adsorption process. The homogeneous distribution of the Zr-G-C_3N_4 nanocomposite constituents (C, O, N, and Zr) shown in Figure 7d–g, while the adsorbed Cu, is clearly observed, as and Figure 7c. This strongly confirms the adsorption of Cu^{2+} onto the composite nanoparticles' surfaces.

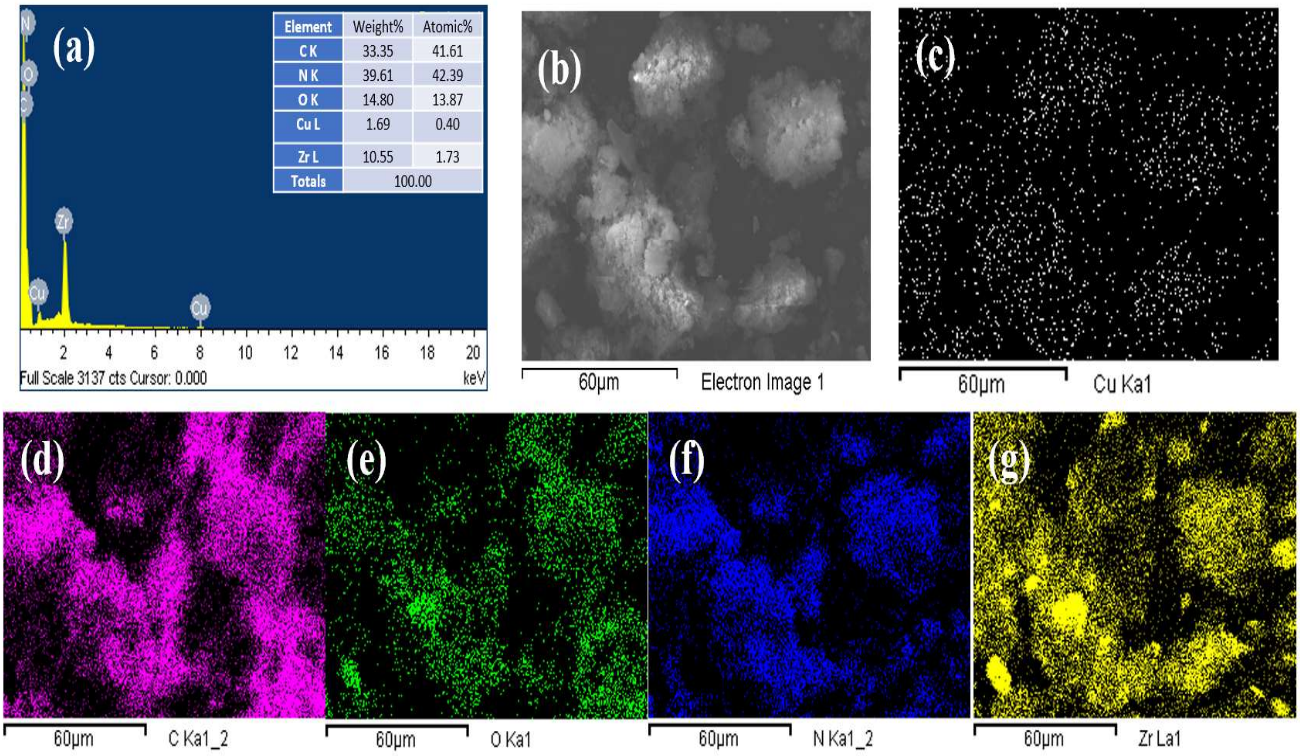

Figure 7. (**a**) EDX spectrum for elements composition; (**b**) SEM image; (**c**–**g**) elemental mapping of C, N, O, and Zr after Cu^{2+} adsorption onto Zr-G-C_3N_4 nanocomposite.

XPS analysis was utilized to investigate the surface chemical composition, the oxidation state of elements on the surface, and the interaction between ZrO_2 and g-C_3N_4. As displayed in Figure 8, the survey scan spectrum contains only the components of N, C, O, and Zr, hence confirming once again the purity of the as-fabricated composite material composed of graphitic carbon nitride and zirconium oxide. The XPS chemical profile spectra of individual fitting of peaks related to Zr, O, C, and N elements are shown in Figure 8. The peaks positioned at 285.7, 288.0, and 289.5 eV for C 1s (Figure 8) correspond to the covalent link of sp^2 hybridized graphic carbon, sp^2 carbon chemically connected to N (N–C=N), and dependence features due to $\pi - \pi$ * excitation, successively [61,62]. Figure 8 displays the distinctive high-resolution peaks for N 1s into the Zr-G-C_3N_4 sorbent at 389.9, and 404.4 eV is related to sp^2 hybridized aromatic N integrated into the triazine structure (C=N–C) and π excitation [63]. The high-resolution peaks for Zr 3d at 182.7 and 185.1 eV may be independently associated with Zr $3d_{5/2}$ and Zr $3d_{3/2}$ [64]. The O 1s spectrum of ZrO_2@g-C_3N_4 displays two peaks around 530.8 eV ascribed to the oxygen (O) crystal structure in zirconium oxide and 532.5 eV corresponding to the materially adsorbed oxygen, as shown in Figure 8 [65,66]. According to the XPS analysis, the Zr-G-C_3N_4 sorbent consists of Zr, O, N, and C, which demonstrates its purity and corroborates the literature [67,68]. The XPS after adsorption revealed a shift in the binding energies for N1s, C1s, and O1s to higher values with a reduction in peak intensities. This may indicate changes in electron clouds around these elements due to coordination with the copper ions. This is in agreement with previous reports of binding Tb to the nitride moiety, as justified by the reduction in the number of =N−C=N−, as a result of the breakage of a C=N π bond and the establishment of a new bond with the metal [69]. Similar results were also reported for Ni and Cr ion complexation interactions with the nitride species [70]. In addition, the adsorption of the Cu ions is validated by the presence of $Cu_{2p3/2}$ and $Cu_{2p1/2}$ peaks at 936.5 and 956.4 eV and an area under the curve ratio of 20,851:111,22 $\approx$ 2:1. Interestingly, the binding energies $Cu_{2p3/2}$ and $Cu_{2p1/2}$ are higher than the respective 932.8 and 952.6 eV values reported for the free ions [71] which may further confirm a successful adsorption process. From the XPS analysis, it can be inferred that the increase in the binding energy of O1s and N1s may be attributable to the coordination of the Cu ions to the N and O on the composite surface that share electrons with the copper ions. The increase in the C1s binding energy is a result of a reduction in the electron densities of neighboring carbons during the complexation of O and N to the metal ions [72]. Thus, strong surface complexation between the electrons present in the functional groups of the composite acting as Lewis bases that interact with the metal ions (Lewis acid) may come about [73].

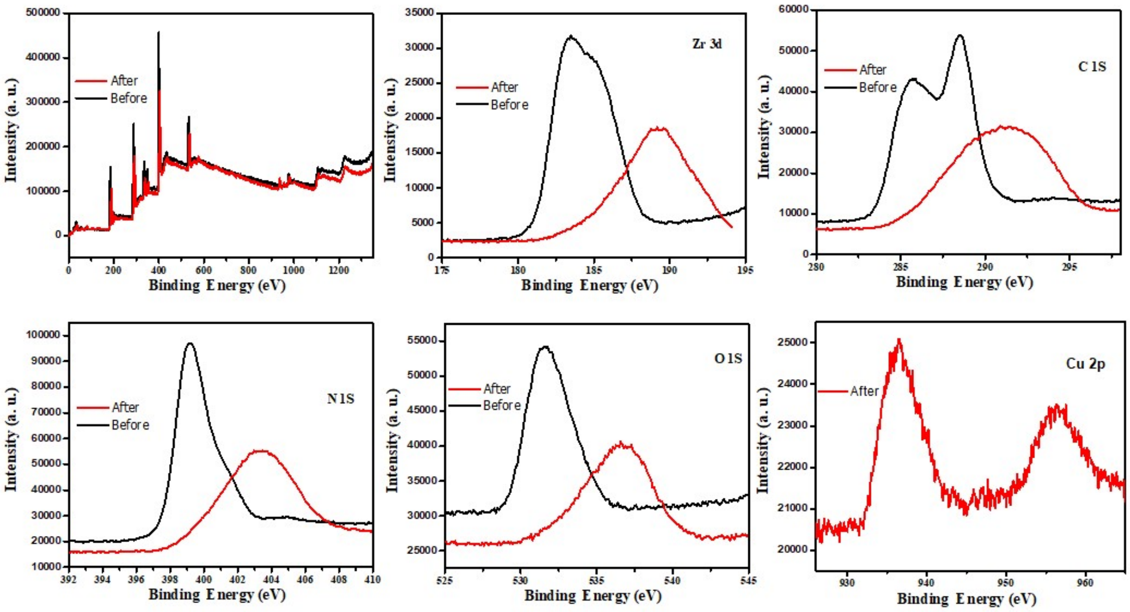

Figure 8. The XPS of the Zr-G-C_3N_4 before and after Cu ions adsorption.

The results obtained by FTIR, XPS, and SEM/EDS elemental mapping demonstrate that functional groups of Zr-G-C_3N_4 (OH, and -NH_2) and p-delocalized electrons of the triazine ring (C_3N_3) are most probably involved in the elimination of Cu (II). The plausible adsorption mechanism of Cu^{2+} ions by Zr-G-C_3N_4 nanomaterial is illustrated in Figure 9.

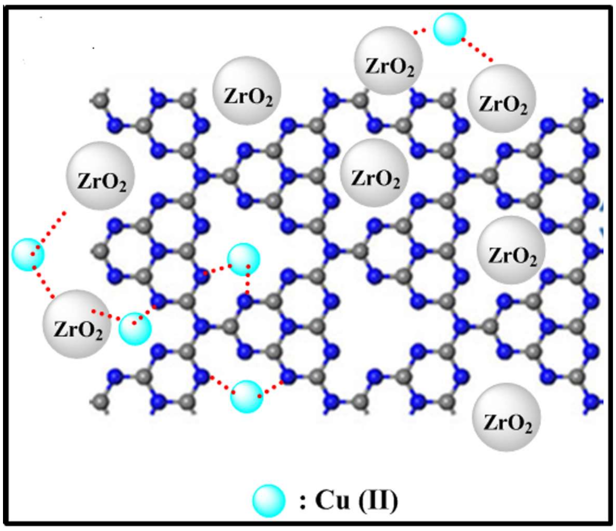

Figure 9. Plausible mechanism for Cu ions adsorption onto Zr-g-C_3N_4 nanoparticles' surface.

3.2.7. Regeneration Tests for Zr-g-C_3N_4 Adsorbent

Desorption analysis was performed to calculate the regeneration capacity of the adsorbent to establish its environmental applicability from an experimental and economic perspective. The reusability and the renewal of an adsorbent such as the Zr-G-C_3N_4 nanomaterial are essential when assessing scale-up and industrial applications. Furthermore, the cyclic reconditioning of this nanosorbent from the physi- or chemisorption reaction medium is vital. After the adsorption investigation, the synthesized nanoparticles were recovered by centrifugation and filtration, thoroughly rinsed with ultrapure hot water, and oven-dried at 105 °C. Afterward, the nanoparticles were soaked with 0.1 M NaOH [74] solution as a desorbing agent in a 50 mL agitated flask (i.e., 500 rpm). This desorbing agent easily releases Cu^{2+} ions from the surface of the Zr-G-C_3N_4 nanocomposite. Accordingly, the collected nanocomposite particles were reutilized for a new removal cycle. Figure 10 illustrates the performance experiment of the adsorption–desorption process for four consecutive cycles. For large-scale applications, the nanoadsorbents can be secured in a meticulous form through lodging in an unyielding support such as a synthetic or natural polymer to guarantee the nanomaterial trapping and nonrelease in the water system. Such arrangement can be adopted to relocate to the fixed-bed column for continuous flow treatment pilots [75–82].

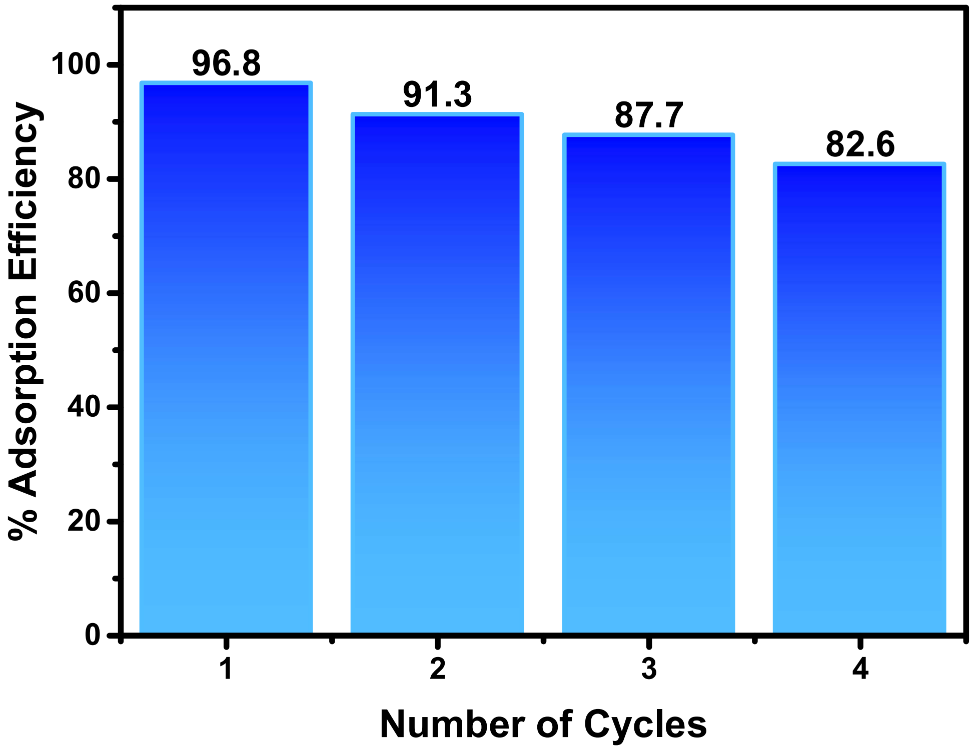

Figure 10. The adsorption–desorption process for four successive cycles.

The Zr-G-C_3N_4 nanocomposite was proven effective for removing Cu^{2+} ions, with an average value of around 88%. This deficiency may be associated with the disrobing agent's despoiler impact and the discharge procedure's weight waste of the nanocomposite [22]. Moreover, this phenomenon can be explained by the decrement in the number of available sites on the surface of the nanomaterial occupied by the adsorbed metal ions [42]. Accordingly, chemisorption was the main mode for the uptake of copper ions onto the nano-adsorbents. Moreover, the stability of the Zr-G-C_3N_4 nano-sorbent was checked by FTIR (Figure 7) after the reusability experiments. The results demonstrate that the FTIR spectrum of nanosorbent continues unmoved following the recycling tests. Thus, the mesoporous Zr-G-C_3N_4 nanocomposite synthesized by a simple-step ultrasonication technique can efficiently and continually eliminate hazardous metal ions from wastewater. Thus, adsorption employing such a composite composed of a metallic center and attached organic functional via robust bonding stands out as a viable, economic, applicable, and reproducible approach [76] for efficient Cu ion removal.

To emphasize the remarkable efficiency of Zr-G-C_3N_4 nanomaterial for the removal of Cu^{2+} ions, a comprehensive comparison with the literature is illustrated in Table 3.

Table 3. Comparison of Cu ion uptake capability by Zr-G-C_3N_4 with other sorbents.

Adsorbents	Cu^{2+} Uptake (mg/g)	t (min)	pH	References
GFLE	193.40	105	1 and 40 °C	[22]
ɣ Fe_2O_3 nanoparticles	26.00	240	6	[77]
Graphene oxide	75.00	1440	<5.95	[59]
MgO-CaO-Al_2O_3 -SiO_2-CO_2 system	16.70	168	-	[78]
MnO_2 nanowires	75.48	30	1.9 to 5.3	[79]
CO_3·Mg-Al LDH	70.7	-	4	[80]
COSAC	17.67	60	5	[45]
Zr-G-C_3N_4	144.1	48	5	This work

3.2.8. Comparative Study

The as-fabricated Zr-G-C_3N_4 mesoporous nanomaterial demonstrates excellent efficiency for the removal of Cu^{2+} metal ions in aqueous solutions (see Table 3).

The as-fabricated nanocomposite exhibits a very high uptake capability of 144.1 mg/g in a relatively shorter time (48 min) under the optimal experimental conditions. This achievement can be explicitly attributed to the material's high surface area (96 m^2/g), nanostructure (50 nm), and mesoporous nature. These findings affirm that the as-fabricated Zr-G-C_3N_4 by a simple and low-cost route can be an effective material for eliminating other potentially organic pollutants and toxic metals [74,75].

4. Conclusions

The present study emphasizes the capability of the mesoporous Zr-G-C_3N_4 sorbent fabricated by a simple ultrasonication route to effectively eliminate the Cu^{2+} metal ions. Adsorption equilibrium isotherms were expressed by Langmuir, Freundlich, and Dubinin–Radushkevich (D-R) adsorption models. The elimination of Cu ions was well fitted by the Langmuir model at a pH of 5.0. The adsorptive capacity of Zr-G-C_3N_4 for copper ions is comparable to—or even better than—many other nanoadsorbents, and surpasses 144 mg/g. The Cu^{2+} ion adsorption was significantly rapid, and the pseudo-second-order rate isotherm better describes the experimental data. The intraparticle diffusion model's results suggest a border coating impact, confirming intraparticle diffusion's role in Cu ions elimination by Zr-G-C_3N_4. In addition, the proven reusability and high regeneration capabilities, even after four adsorption–desorption cycles indicate the feasibility for the Cu ions' adsorption onto the Zr-G-C_3N_4 nanosorbent. Based on the obtained results, the produced nanoadsorbents have the potential to be used as suitable adsorbents for eliminating Cu^{2+} ions.

Author Contributions: L.K. and A.M.: conceptualization and methodology; L.K., A.M. and N.B.H.: writing—original draft preparation; L.K., A.M., K.K.T., N.B.H. and M.B.: writing—review and editing; L.K., A.A.A. and M.B.: supervision and editing. All authors have read and agreed to the published version of the manuscript.

Funding: This research received no external funding.

Data Availability Statement: Not applicable.

Acknowledgments: The authors extend their appreciation to the Deanship of Scientific Research at Imam Mohammad Ibn Saud Islamic University (IMSIU) for funding and supporting this work through Research Partnership Program no RP-21-09-66.

Conflicts of Interest: The authors declare no conflict of interest.

References

1. Anbia, M.; Ghassemian, Z. Removal of Cd(II) and Cu(II) from aqueous solutions using mesoporous silicate containing zirconium and iron. *Chem. Eng. Res. Des.* **2011**, *89*, 2770–2775. [CrossRef]
2. Anbia, M.; Haqshenas, M. Adsorption studies of Pb(II) and Cu(II) ions on mesoporous carbon nitride functionalized with melamine-based dendrimer amine. *Int. J. Environ. Sci. Technol.* **2015**, *12*, 2649–2664. [CrossRef]
3. Teodoro, F.S.; Soares, L.C.; Filgueiras, J.G.; de Azevedo, E.R.; Patiño-Agudelo, J.; Adarme, O.F.H.; da Silva, L.H.M.; Gurgel, L.V.A. Batch and continuous adsorption of Cu(II) and Zn(II) ions from aqueous solution on bi-functionalized sugarcane-based biosorbent. *Environ. Sci. Pollut. Res.* **2021**, *29*, 26425–26448. [CrossRef] [PubMed]
4. Wang, R.-H.; Zhu, X.-F.; Qian, W.; Yu, Y.-C.; Xu, R.-K. Effect of pectin on adsorption of Cu(II) by two variable-charge soils from southern China. *Environ. Sci. Pollut. Res.* **2015**, *22*, 19687–19694. [CrossRef]
5. Meng, J.; Feng, X.; Dai, Z.; Liu, X.; Wu, J.; Xu, J. Adsorption characteristics of Cu(II) from aqueous solution onto biochar derived from swine manure. *Environ. Sci. Pollut. Res.* **2014**, *21*, 7035–7046. [CrossRef]
6. Dong, J.; Du, Y.; Duyu, R.; Shang, Y.; Zhang, S.; Han, R. Adsorption of copper ion from solution by polyethylenimine modified wheat straw. *Bioresour. Technol. Rep.* **2019**, *6*, 96–102. [CrossRef]
7. Trikkaliotis, D.G.; Christoforidis, A.K.; Mitropoulos, A.C.; Kyzas, G.Z. Adsorption of copper ions onto chitosan/poly(vinyl alcohol) beads functionalized with poly(ethylene glycol). *Carbohydr. Polym.* **2020**, *234*, 115890. [CrossRef]
8. Khan, J.; Lin, S.; Nizeyimana, J.C.; Wu, Y.; Wang, Q.; Liu, X. Removal of copper ions from wastewater via adsorption on modified hematite (α-Fe_2O_3) iron oxide coated sand. *J. Clean. Prod.* **2021**, *319*, 128687. [CrossRef]
9. Ye, X.; Shang, S.; Zhao, Y.; Cui, S.; Zhong, Y.; Huang, L. Ultra-efficient adsorption of copper ions in chitosan–montmorillonite composite aerogel at wastewater treatment. *Cellulose* **2021**, *28*, 7201–7212. [CrossRef]
10. Su, C.; Berekute, A.K.; Yu, K.-P. Chitosan@ TiO_2 composites for the adsorption of copper (II) and antibacterial applications. *Sustain. Environ. Res.* **2022**, *32*, 1–15. [CrossRef]
11. Reddad, Z.; Gerente, C.; Andres, Y.; Le Cloirec, P. Adsorption of Several Metal Ions onto a Low-Cost Biosorbent: Kinetic and Equilibrium Studies. *Environ. Sci. Technol.* **2002**, *36*, 2067–2073. [CrossRef] [PubMed]
12. Gavrilescu, M. Removal of Heavy Metals from the Environment by Biosorption. *Eng. Life Sci.* **2004**, *4*, 219–232. [CrossRef]
13. Wan, J.; Chen, L.; Li, Q.; Ye, Y.; Feng, X.; Zhou, A.; Long, X.; Xia, D.; Zhang, T.C. A novel hydrogel for highly efficient adsorption of Cu (II): Synthesis, characterization, and mechanisms. *Environ. Sci. Pollut. Res.* **2020**, *27*, 26621–26630. [CrossRef] [PubMed]
14. Al-Saydeh, S.A.; El-Naas, M.H.; Zaidi, S.J. Copper removal from industrial wastewater: A comprehensive review. *J. Ind. Eng. Chem.* **2017**, *56*, 35–44. [CrossRef]
15. Liu, Y.-L.; Yang, L.; Li, P.; Li, S.-J.; Li, L.; Pang, X.-X.; Ye, F.; Fu, Y. A novel colorimetric and "turn-off" fluorescent probe based on catalyzed hydrolysis reaction for detection of Cu2+ in real water and in living cells. *Spectrochim. Acta Part A Mol. Biomol. Spectrosc.* **2020**, *227*, 117540. [CrossRef]
16. Ismael, M. A review on graphitic carbon nitride (g-C3N4) based nanocomposites: Synthesis, categories, and their application in photocatalysis. *J. Alloys Compd.* **2020**, *846*, 156446. [CrossRef]
17. Obregón, S. Exploring nanoengineering strategies for the preparation of graphitic carbon nitride nanostructures. *FlatChem* **2023**, *38*, 100473. [CrossRef]
18. Zhang, M.; Yang, Y.; An, X.; Hou, L.-A. A critical review of g-C3N4-based photocatalytic membrane for water purification. *Chem. Eng. J.* **2021**, *412*, 128663. [CrossRef]
19. Shahbazi, A.; Younesi, H.; Badiei, A. Functionalized SBA-15 mesoporous silica by melamine-based dendrimer amines for adsorptive characteristics of Pb (II), Cu (II) and Cd (II) heavy metal ions in batch and fixed bed column. *Chem. Eng. J.* **2011**, *168*, 505–518. [CrossRef]
20. Khezami, L.; Elamin, N.; Modwi, A.; Taha, K.K.; Amer, M.S.; Bououdina, M. Mesoporous Sn@ TiO_2 nanostructures as excellent adsorbent for Ba ions in aqueous solution. *Ceram. Int.* **2022**, *48*, 5805–5813. [CrossRef]
21. Mustafa, B.; Modwi, A.; Ismail, M.; Makawi, S.; Hussein, T.; Abaker, Z.; Khezami, L. Adsorption performance and Kinetics study of Pb(II) by RuO_2–ZnO nanocomposite: Construction and Recyclability. *Int. J. Environ. Sci. Technol.* **2022**, *19*, 327–340. [CrossRef]
22. Abdulkhair, B.; Salih, M.; Modwi, A.; Adam, F.; Elamin, N.; Seydou, M.; Rahali, S. Adsorption behavior of barium ions onto ZnO surfaces: Experiments associated with DFT calculations. *J. Mol. Struct.* **2021**, *1223*, 128991. [CrossRef]
23. Ghiloufi, I.; El Ghoul, J.; Modwi, A.; El Mir, L. Ga-doped ZnO for adsorption of heavy metals from aqueous solution. *Mater. Sci. Semicond. Process.* **2016**, *42*, 102–106. [CrossRef]
24. Modwi, A.; Khezami, L.; Taha, K.; Al-Duaij, O.; Houas, A. Fast and high efficiency adsorption of Pb(II) ions by Cu/ZnO composite. *Mater. Lett.* **2017**, *195*, 41–44. [CrossRef]

25. Khezami, L.; Taha, K.K.; Modwi, A. Efficient Removal of Cobalt from Aqueous Solution by Zinc Oxide Nanoparticles: Kinetic and Thermodynamic Studies. *Z. Nat. A* **2017**, *72*, 409–418. [CrossRef]
26. Khezami, L.; Modwi, A.; Ghiloufi, I.; Taha, K.K.; Bououdina, M.; ElJery, A.; El Mir, L. Effect of aluminum loading on structural and morphological characteristics of ZnO nanoparticles for heavy metal ion elimination. *Environ. Sci. Pollut. Res.* **2020**, *27*, 3086–3099. [CrossRef] [PubMed]
27. Singh, J.; Singh, S.; Gill, R. Applications of biopolymer coatings in biomedical engineering. *J. Electrochem. Sci. Eng.* **2022**, *13*, 63–81. [CrossRef]
28. Nevarez-Rascon, A.; González-Lopez, S.; Acosta-Torres, L.S.; Nevarez-Rascon, M.M.; Borunda, E.O. Synthesis, biocompatibility and mechanical properties of ZrO2-Al2O3 ceramics composites. *Dent. Mater. J.* **2016**, *35*, 392–398. [CrossRef]
29. Sayed, E.T.; Abdelkareem, M.A.; Alawadhi, H.; Elsaid, K.; Wilberforce, T.; Olabi, A. Graphitic carbon nitride/carbon brush composite as a novel anode for yeast-based microbial fuel cells. *Energy* **2021**, *221*, 119849. [CrossRef]
30. Svoboda, L.; Bednář, J.; Dvorský, R.; Panáček, A.; Hochvaldová, L.; Kvítek, L.; Malina, T.; Konvičková, Z.; Henych, J.; Němečková, Z.; et al. Crucial cytotoxic and antimicrobial activity changes driven by amount of doped silver in biocompatible carbon nitride nanosheets. *Colloids Surf. B Biointerfaces* **2021**, *202*, 111680. [CrossRef]
31. Xavier, J.R. Electrochemical and Mechanical Investigation of Newly Synthesized NiO-ZrO 2 Nanoparticle–Grafted Polyure-thane Nanocomposite Coating on Mild Steel in Chloride Media. *J. Mater. Eng. Perform.* **2021**, *30*, 1554–1566. [CrossRef]
32. Channu, V.R.; Kalluru, R.R.; Schlesinger, M.; Mehring, M.; Holze, R. Synthesis and characterization of ZrO2 nanoparticles for optical and electrochemical applications. *Colloids Surf. A Physicochem. Eng. Asp.* **2011**, *386*, 151–157. [CrossRef]
33. Yu, Y.; Yan, W.; Wang, X.; Li, P.; Gao, W.; Zou, H.; Wu, S.; Ding, K. Surface engineering for extremely enhanced charge separation and photocatalytic hydrogen evolution on g-C3N4. *Adv. Mater.* **2018**, *30*, 1705060. [CrossRef] [PubMed]
34. Gonçalves, N.; Carvalho, J.; Lima, Z.; Sasaki, J. Size–strain study of NiO nanoparticles by X-ray powder diffraction line broadening. *Mater. Lett.* **2012**, *72*, 36–38. [CrossRef]
35. Wang, X.; Wang, S.; Hu, W.; Cai, J.; Zhang, L.; Dong, L.; Zhao, L.; He, Y. Synthesis and photocatalytic activity of SiO_2/g-C_3N_4 composite photocatalyst. *Mater. Lett.* **2014**, *115*, 53–56. [CrossRef]
36. Modwi, A.; Abbo, M.A.; Hassan, E.A.; Houas, A. Effect of annealing on physicochemical and photocatalytic activity of Cu5% loading on ZnO synthesized by sol–gel method. *J. Mater. Sci. Mater. Electron.* **2016**, *27*, 12974–12984. [CrossRef]
37. Lagergren, S.K. About the theory of so-called adsorption of soluble substances. *Sven. Vetenskapsakad. Handingarl.* **1898**, *24*, 1–39.
38. Abdelrahman, E.A.; El-Reash, Y.A.; Youssef, H.M.; Kotp, Y.H.; Hegazey, R. Utilization of rice husk and waste aluminum cans for the synthesis of some nanosized zeolite, zeolite/zeolite, and geopolymer/zeolite products for the efficient removal of Co(II), Cu(II), and Zn(II) ions from aqueous media. *J. Hazard. Mater.* **2021**, *401*, 123813. [CrossRef]
39. Chien, S.H.; Clayton, W.R. Application of Elovich Equation to the Kinetics of Phosphate Release and Sorption in Soils. *Soil Sci. Soc. Am. J.* **1980**, *44*, 265–268. [CrossRef]
40. Ali, I.; Peng, C.; Ye, T.; Naz, I. Sorption of cationic malachite green dye on phytogenic magnetic nanoparticles functionalized by 3-marcaptopropanic acid. *RSC Adv.* **2018**, *8*, 8878–8897. [CrossRef]
41. Wang, X.; Cai, W.; Lin, Y.; Wang, G.; Liang, C. Mass production of micro/nanostructured porous ZnO plates and their strong structurally enhanced and selective adsorption performance for environmental remediation. *J. Mater. Chem.* **2010**, *20*, 8582. [CrossRef]
42. Acharya, J.; Sahu, J.; Mohanty, C.; Meikap, B. Removal of lead(II) from wastewater by activated carbon developed from Tamarind wood by zinc chloride activation. *Chem. Eng. J.* **2009**, *149*, 249–262. [CrossRef]
43. Ahmad, M.A.; Rahman, N.K. Equilibrium, kinetics and thermodynamic of Remazol Brilliant Orange 3R dye adsorption on coffee husk-based activated carbon. *Chem. Eng. J.* **2011**, *170*, 154–161. [CrossRef]
44. Kumar, K.V.; Ramamurthi, V.; Sivanesan, S. Biosorption of malachite green, a cationic dye onto Pithophora sp., a fresh water algae. *Dye. Pigment.* **2006**, *69*, 102–107. [CrossRef]
45. Podder, M.; Majumder, C. Biosorption of As (III) and As (V) on the surface of TW/$MnFe_2O_4$ composite from wastewater: Kinetics, mechanistic and thermodynamics. *Appl. Water Sci.* **2017**, *7*, 2689–2715. [CrossRef]
46. Ismail, M.; Jobara, A.; Bekouche, H.; Allateef, M.A.; Ben Aissa, M.A.; Modwi, A. Impact of Cu Ions removal onto MgO nanostructures: Adsorption capacity and mechanism. *J. Mater. Sci. Mater. Electron.* **2022**, *33*, 12500–12512. [CrossRef]
47. Brdar, M.; Šćiban, M.; Takači, A.; Došenović, T. Comparison of two and three parameters adsorption isotherm for Cr(VI) onto Kraft lignin. *Chem. Eng. J.* **2012**, *183*, 108–111. [CrossRef]
48. Freundlich, H. Over the adsorption in solution. *J. Phys. Chem.* **1906**, *57*, 1100–1107.
49. Temkin, M.I. Adsorption equilibrium and the kinetics of processes on nonhomogeneous surfaces and in the interaction between adsorbed molecules. *Zh. Fiz. Chim.* **1941**, *15*, 296–332.
50. Dubinin, M. The equation of the characteristic curve of activated charcoal. *Dokl. Akad. Nauk. SSSR.* **1947**, *55*, 327–329.
51. Hu, Q.; Zhang, Z. Application of Dubinin–Radushkevich isotherm model at the solid/solution interface: A theoretical analysis. *J. Mol. Liq.* **2019**, *277*, 646–648. [CrossRef]
52. Nikiforova, T.E.; Kozlov, V.A.; Telegin, F.Y. Chemisorption of copper ions in aqueous acidic solutions by modified chitosan. *Mater. Sci. Eng. B* **2021**, *263*, 114778. [CrossRef]
53. Bae, M.; Lee, H.; Yoo, K.; Kim, S. Copper(I) selective chemisorption on magnetite (Fe_3O_4) over gold(I) ions in chloride solution with cyanide. *Hydrometallurgy* **2021**, *201*, 105560. [CrossRef]

54. Gao, X.; Wu, L.; Xu, Q.; Tian, W.; Li, Z.; Kobayashi, N. Adsorption kinetics and mechanisms of copper ions on activated carbons derived from pinewood sawdust by fast H_3PO_4 activation. *Environ. Sci. Pollut. Res.* **2018**, *25*, 7907–7915. [CrossRef] [PubMed]
55. Buema, G.; Trifas, L.-M.; Harja, M. Removal of Toxic Copper Ion from Aqueous Media by Adsorption on Fly Ash-Derived Zeolites: Kinetic and Equilibrium Studies. *Polymers* **2021**, *13*, 3468. [CrossRef] [PubMed]
56. Kumar, G.P.; Kumar, P.A.; Chakraborty, S.; Ray, M. Uptake and desorption of copper ion using functionalized polymer coated silica gel in aqueous environment. *Sep. Purif. Technol.* **2007**, *57*, 47–56. [CrossRef]
57. Salam, M.A.; Al-Zhrani, G.; Kosa, S.A. Simultaneous removal of copper (II), lead (II), zinc (II) and cadmium (II) from aqueous solutions by multi-walled carbon nanotubes. *Comptes Rendus Chim.* **2012**, *15*, 398–408. [CrossRef]
58. Toscano, G.; Caristi, C.; Cimino, G. Sorption of heavy metal from aqueous solution by volcanic ash. *Comptes Rendus Chim.* **2008**, *11*, 765–771. [CrossRef]
59. Ren, X.; Li, J.; Tan, X.; Wang, X. Comparative study of graphene oxide, activated carbon and carbon nanotubes as adsorbents for copper de-contamination. *Dalton Trans.* **2013**, *42*, 5266–5274. [CrossRef]
60. Bohli, T.; Ouederni, A.; Fiol, N.; Villaescusa, I. Evaluation of an activated carbon from olive stones used as an adsorbent for heavy metal removal from aqueous phases. *Comptes Rendus Chim.* **2015**, *18*, 88–99. [CrossRef]
61. Mao, N.; Jiang, J.-X. MgO/g-C_3N_4 nanocomposites as efficient water splitting photocatalysts under visible light irradiation. *Appl. Surf. Sci.* **2019**, *476*, 144–150. [CrossRef]
62. Ge, L.; Han, C. Synthesis of MWNTs/g-C_3N_4 composite photocatalysts with efficient visible light photocatalytic hydrogen evolution activity. *Appl. Catal. B Environ.* **2012**, *117-118*, 268–274. [CrossRef]
63. Ji, H.; Chang, F.; Hu, X.; Qin, W.; Shen, J. Photocatalytic degradation of 2,4,6-trichlorophenol over g-C_3N_4 under visible light irradiation. *Chem. Eng. J.* **2013**, *218*, 183–190. [CrossRef]
64. Velu, S.; Suzuki, K.; Gopinath, C.S.; Yoshida, H.; Hattori, T.X.P.S. XPS, XANES and EXAFS investigations of CuO/ZnO/Al_2O_3/ZrO_2 mixed oxide catalysts. *Phys. Chem. Chem. Phys.* **2002**, *4*, 1990–1999. [CrossRef]
65. Ragupathy, P.; Park, D.H.; Campet, G.; Vasan, H.N.; Hwang, S.-J.; Choy, J.-H.; Munichandraiah, N. Remarkable Capacity Retention of Nanostructured Manganese Oxide upon Cycling as an Electrode Material for Supercapacitor. *J. Phys. Chem. C* **2009**, *113*, 6303–6309. [CrossRef]
66. Toghan, A.; Modwi, A. Boosting unprecedented indigo carmine dye photodegradation via mesoporous MgO@ g-C_3N_4 nanocomposite. *J. Photochem. Photobiol. A Chem.* **2021**, *419*, 113467. [CrossRef]
67. Muhmood, T.; Xia, M.; Lei, W.; Wang, F.; Khan, M.A. Efficient and stable ZrO_2/Fe modified hollow-C 3 N 4 for photodegradation of the herbicide MTSM. *RSC Adv.* **2017**, *7*, 3966–3974. [CrossRef]
68. Ismael, M.; Wu, Y.; Wark, M. Photocatalytic activity of ZrO_2 composites with graphitic carbon nitride for hydrogen production under visible light. *New J. Chem.* **2019**, *43*, 4455–4462. [CrossRef]
69. Liu, X.; Zhang, S.; Liu, J.; Wei, X.; Yang, T.; Chen, M.; Wang, J. Rare-Earth Doping Graphitic Carbon Nitride Endows Distinctive Multiple Emissions with Large Stokes Shifts. *CCS Chem.* **2022**, *4*, 1990–1999. [CrossRef]
70. Guo, J.; Chen, T.; Zhou, X.; Xia, W.; Zheng, T.; Zhong, C.; Liu, Y. Synthesis, Cr(VI) removal performance and mechanism of nanoscale zero-valent iron modified potassium-doped graphitic carbon nitride. *Water Sci. Technol.* **2020**, *81*, 1840–1851. [CrossRef]
71. Zou, X.; Silva, R.; Goswami, A.; Asefa, T. Cu-doped carbon nitride: Bio-inspired synthesis of H2-evolving electrocatalysts using graphitic carbon nitride (g-C_3N_4) as a host material. *Appl. Surf. Sci.* **2015**, *357*, 221–228. [CrossRef]
72. Zhang, L.; Guo, J.; Huang, X.; Wang, W.; Sun, P.; Li, Y.; Han, J. Functionalized biochar-supported magnetic $MnFe_2O_4$ nanocomposite for the removal of Pb (ii) and Cd (ii). *RSC Adv.* **2019**, *9*, 365–376. [CrossRef] [PubMed]
73. Shen, C.; Chen, C.; Wen, T.; Zhao, Z.; Wang, X.; Xu, A. Superior adsorption capacity of g-C_3N_4 for heavy metal ions from aqueous solutions. *J. Colloid Interface Sci.* **2015**, *456*, 7–14. [CrossRef]
74. Awual, M.R.; Yaita, T.; Suzuki, S.; Shiwaku, H. Ultimate selenium (IV) monitoring and removal from water using a new class of organic ligand based composite adsorbent. *J. Hazard. Mater.* **2015**, *291*, 111–119. [CrossRef] [PubMed]
75. Aziz, F.; El Achaby, M.; Lissaneddine, A.; Aziz, K.; Ouazzani, N.; Mamouni, R.; Mandi, L. Composites with alginate beads: A novel design of nano-adsorbents impregnation for large-scale continuous flow wastewater treatment pilots. *Saudi J. Biol. Sci.* **2020**, *27*, 2499–2508. [CrossRef]
76. Şimşek, S.; Derin, Y.; Kaya, S.; Şenol, Z.M.; Katin, K.P.; Özer, A.; Tutar, A. High-performance material for the effective removal of uranyl ion from solution: Computationally sup-ported experimental studies. *Langmuir* **2022**, *38*, 10098–10113. [CrossRef] [PubMed]
77. Ozdemir, S.; Turkan, Z.; Kilinc, E.; Bayat, R.; Soylak, M.; Sen, F. Preconcentrations of Cu (II) and Mn (II) by magnetic solid-phase extraction on Bacillus cereus loaded γ-Fe2O3 nanomaterials. *Environ. Res.* **2022**, *209*, 112766. [CrossRef]
78. Morozova, A.G.; Lonzinger, T.M.; Skotnikov, V.A.; Mikhailov, G.G.; Kapelyushin, Y.; Khandaker, M.U.; Alqahtani, A.; Bradley, D.A.; Sayyed, M.I.; Tishkevich, D.I.; et al. Insights into sorption–mineralization mechanism for sustainable granular composite of MgO-CaO-Al_2O_3-SiO_2-CO_2 based on nanosized adsorption centers and its effect on aqueous Cu (II) removal. *Nanomaterials* **2021**, *12*, 116. [CrossRef]
79. Claros, M.; Kuta, J.; El-Dahshan, O.; Michalička, J.; Jimenez, Y.P.; Vallejos, S. Hydrothermally synthesized MnO_2 nanowires and their application in Lead (II) and Copper (II) batch ad-sorption. *J. Mol. Liq.* **2021**, *325*, 115203. [CrossRef]

80. Baaloudj, O.; Nasrallah, N.; Kebir, M.; Guedioura, B.; Amrane, A.; Nguyen-Tri, P.; Nanda, S.; Assadi, A.A. Artificial neural network modeling of cefixime photodegradation by synthesized $CoBi_2O_4$ na-noparticles. *Environ. Sci. Pollut. Res.* **2021**, *28*, 15436–15452. [CrossRef]
81. Azzaz, A.A.; Jellali, S.; Akrout, H.; Assadi, A.A.; Bousselmi, L. Dynamic investigations on cationic dye desorption from chemically modified lignocellulosic material using a low-cost eluent: Dye recovery and anodic oxidation efficiencies of the desorbed solutions. *J. Clean. Prod.* **2018**, *201*, 28–38. [CrossRef]
82. Yang, X.; Kameda, T.; Saito, Y.; Kumagai, S.; Yoshioka, T. Investigation of the mechanism of Cu(II) removal using Mg-Al layered double hydroxide intercalated with carbonate: Equilibrium and pH studies and solid-state analyses. *Inorg. Chem. Commun.* **2021**, *132*, 108839. [CrossRef]